Journal of Thermal Biology 115 (2023) 103613

Contents lists available at ScienceDirect

Journal of Thermal Biology

journal homepage: www.elsevier.com/locate/jtherbio

Incorporating species-specific morphology improves model predictions of thermal and hydric stress in the sand fiddler crab, *Leptuca pugilator*

Paul D. Mathewson [a,*], M. Zachary Darnell [b], Zachary M. Lane [b], Talene G. Yeghissian [b], Jeffrey Levinton [c], Warren P. Porter [a]

[a] Department of Integrative Biology, University of Wisconsin–Madison, Madison, WI, USA
[b] Division of Coastal Sciences, School of Ocean Science and Engineering, The University of Southern Mississippi, Ocean Springs, MS, USA
[c] Department of Ecology and Evolution, Stony Brook University, Stony Brook, NY, USA

ARTICLE INFO

Keywords:
Biophysical model
Leptuca pugilator
Fiddler crab
Niche mapper
Thermoregulation
Water loss

ABSTRACT

Understanding where and why organisms are experiencing thermal and hydric stress is critical for predicting species' responses to climate change. Biophysical models that explicitly link organismal functional traits like morphology, physiology, and behavior to environmental conditions can provide valuable insight into determinants of thermal and hydric stress. Here we use a combination of direct measurements, 3D modeling, and computational fluid dynamics to develop a detailed biophysical model of the sand fiddler crab, *Leptuca pugilator*. We compare the detailed model's performance to a model using a simpler ellipsoidal approximation of a crab. The detailed model predicted crab body temperatures within 1 °C of observed in both laboratory and field settings; the ellipsoidal approximation model predicted body temperatures within 2 °C of observed body temperatures. Model predictions are meaningfully improved through efforts to incorporate species-specific morphological properties rather than relying on simple geometric approximations. Experimental evaporative water loss (EWL) measurements indicate that *L. pugilator* can modify its permeability to EWL as a function of vapor density gradients, providing novel insight into physiological thermoregulation in the species. Body temperature and EWL predictions made over the course of a year at a single site demonstrate how such biophysical models can be used to explore mechanistic drivers and spatiotemporal patterns of thermal and hydric stress, providing insight into current and future distributions in the face of climate change.

1. Introduction

Climate change is an important threat facing biodiversity around the globe (Thomas et al., 2004; Wiens, 2016; Pecl et al., 2017). Climate change can impact animals through a variety of direct and indirect mechanisms. For example, increased thermal stress associated with climate change may have direct physiological effects on an organism, limiting its performance or restricting its activity. Increased thermal stress can also indirectly impact organisms by altering resource availability, interspecific interactions, or disease spread (Cahill et al., 2013; Ockendon et al., 2014; Sonn et al., 2020).

An important ecological, management, and conservation challenge is predicting how species might respond to this climate change. Biophysical models facilitate exploration of how an animal's morphology, physiology, and behavior interact with its environment in terms of energy, dry mass and water balances to affect fitness and performance using fundamental principles of heat and mass transfer (Porter and Gates, 1969; Porter et al., 1973; Kearney and Porter, 2009). Thus, biophysical models can be useful tools to predict thermal stress in animals in both current and future climates and investigate the potential impact climate change could have on performance (Mouquet et al., 2015; Urban et al., 2016; Briscoe et al., 2023).

As with all models, biophysical models represent a trade-off between accuracy and simplifying assumptions due to lack of more specific information (O'Connor and Spotila, 1992; Dudley et al., 2013). One common simplifying approximation made in biophysical animal models is approximating the animal as a simple geometric shape such as a sphere, ellipsoid, or cylinder for the purposes of computing the animal's heat and mass transfer properties. Traditionally, determining heat transfer properties specific to a given animal morphology involved creating a metal casting and placing the casting in a wind tunnel (e.g., Porter et al., 1973). An alternative approach that is potentially more

* Corresponding author. Department of Integrative Biology, University of Wisconsin, 250 North Mills Street, Madison, WI, 53706, USA.
E-mail address: mathewson@wisc.edu (P.D. Mathewson).

https://doi.org/10.1016/j.jtherbio.2023.103613
Received 3 June 2022; Received in revised form 3 June 2023; Accepted 4 June 2023
Available online 22 June 2023

accessible and versatile is using 3D modeling and computational fluid dynamics software.

Dudley et al. (2013) demonstrate how CFD-derived heat transfer properties are in good agreement with experimentally-derived properties for animal morphologies and how classical approximations with simple geometries differ substantially. Here, we extend the work of Dudley et al. (2013, 2016) by using observational data from live animals to evaluate the performance of biophysical models built using heat and mass transfer properties derived from CFD. We also compare performance of this model to one relying on a simpler ellipsoidal approximation of the animal to investigate the value of more detailed models.

Sand fiddler crabs (*Leptuca pugilator*) are an excellent model organism for this investigation due to their highly complex morphology that could potentially cause meaningful differences in heat and mass transfer properties from a simple geometric approximation. Additionally, due to their resource-defense reproductive strategy and stressful habitat, biophysical models could provide useful insight into *L. pugilator*'s ecology, evolution and response to climate change. *L. pugilator* is a small (2–5 g) semi-terrestrial inhabitant of protected sandy shorelines along the North American Atlantic and Gulf of Mexico coasts (Crane, 1975). For organisms inhabiting the marine intertidal zone such as the fiddler crab, desiccation and thermal stress are considered the most important abiotic limits on fitness and performance (Thurman, 1998; Allen et al., 2012).

Leptuca pugilator's territory defense and courtship occurs primarily in the hot, dry intertidal zones of open sand shorelines, where males engage in waving displays with an enlarged major claw to attract females to their mating burrows (Smith and Miller, 1973; Hyatt and Salmon, 1978; Christy, 1982a). Burrow defense and mate attractions occurs in the summer when environmental temperatures in the high intertidal zone frequently exceed preferred body temperature (T_b), subjecting males to both desiccation and thermal stress (Christy, 1982b; Allen et al., 2012: Allen and Levinton, 2014).

The most effective ways for fiddler crabs to avoid overheating is to retreat into a burrow or cool the body through evaporative water loss (EWL) (Smith and Miller, 1973; Munguia et al., 2017). However, EWL will allow the male to maintain activity only until it loses too much water, at which point it will need to retreat to the burrow to rehydrate. Similarly, retreat to the burrow is highly effective, but also costly, as a retreat to the burrow requires a cessation of courtship behavior. Thus, crabs are faced with the tradeoff of remaining at the surface longer and risking decreased performance as their T_b and desiccation increase or spending more time in the burrow cooling off and rehydrating at the expense of reduced time to attract females (Allen and Levinton, 2014; Darnell et al., 2020). Field evidence demonstrates that *L. pugilator* males maintain a hydrated state under conditions of heat and desiccation stress, suggesting frequent retreats to maintain a high level of hydration even in stressful condition (Levinton et al., 2015).

Niche Mapper (hereafter "NM"), a biophysical modeling software package, has previously been used to model environmental constraints on the distribution of various ectotherms, including leatherback sea turtles (*Dermochelys coriacea;* Dudley et al., 2016), wood frog (*Lithobates sylvaticus*; HYPERFitzpatrick et al., 2019; 2020), grass lizard (*Takydromus hsuehshanensis;* Huang et al., 2014), cane toad (*Bufo marinus*; Kearney et al., 2008), and Australian sleepy lizard (*Tiliqua rugosa;* Kearney et al., 2018).

Here we compare the performance of two NM models developed for fiddler crabs: one built using 3D modeling and CFD software to calculate heat and mass transfer properties specific to the crab's morphology and one built using an ellipsoidal approximation. We then evaluate the two models' T_b and evaporative water loss predictions against empirical data. Finally, we demonstrate how a biophysical model can be used to provide mechanistic insight into how local environmental conditions interact with the species' morphology and physiology to determine the extent of thermal and hydric stress experienced by the animal.

2. Methods

2.1. Niche Mapper introduction

Niche Mapper ("NM") is a biophysical modeling software package consisting of two submodels: (1) a microclimate submodel that calculates microclimate conditions, and (2) an animal submodel that performs heat and mass balance calculations based on animal properties and its microclimate conditions.

We used NicheMapR, version 1.2 (Kearney and Porter, 2017), which is an implementation of the microclimate model developed for the R programming language (R Development Core Team 2016). The microclimate submodel operation has previously been described in detail (Kearney and Porter, 2017) and tested for ability to accurately predict microclimate conditions in marine beach environments (Fuentes and Porter, 2013; Bentley et al., 2020). Briefly, the microclimate submodel uses macroclimate data (maximum and minimum daily air temperatures, relative humidity, cloud cover, and wind speed), substrate properties, vegetative cover, geographic location, topography, and time of year to calculate hourly microclimate conditions an animal experiences at any point from 2 m above ground to 2 m below ground. Separate environmental profiles are calculated for open and shaded microenvironments.

The ectotherm submodel uses local microclimate information in conjunction with morphological, physiological, and behavioral information about the animal to solve coupled heat and mass balances and calculate the animal's core body temperature (T_b) and evaporative water loss (EWL) on an hourly basis, accounting for metabolic heat production (Q_{met}) and convective (Q_{conv}), conductive (Q_{cond}), radiative (Q_{IR}), evaporative (Q_{evap}), and solar (Q_{sol}) heat fluxes with its microclimate (See Kearney and Porter (2020) for code and full equations). Steady state T_b calculations are made using the following equation:

$$Q_{met} + Q_{sol} + Q_{IR,in} = Q_{evap} + Q_{IR,out} + Q_{conv} + Q_{cond} \quad \text{Eq. 1}$$

On an hourly basis throughout a model day, the microclimate submodel calculates microclimate conditions the model animal is subject to for heat exchange. The ectotherm submodel then solves Eq. (1) by iteratively guessing for a T_b that will satisfy the heat balance given the animal's properties and the microclimate conditions.

2.2. Microclimate submodel parameterization and validation

We collected data necessary to parameterize and validate the microclimate submodel in Beaufort, NC, USA (July 19-21, 2019), Panacea, FL, USA (June 22-25, 2021) and Stonybrook, NY, USA (June 22-23, 2022). Data were collected with a weather station positioned in the upper intertidal or supratidal zones in areas where active fiddler crab burrows were observed. Data were collected on a datalogger (Campbell Scientific 21x Micrologger; Logan, UT) and subsequently transferred to a computer.

Air temperatures were concurrently collected using shielded thermocouples placed near the ground surface (0.03–0.04 m), ~0.5 m, ~1 m, and ~2 m above the ground. Sand surface temperatures were measured using iButtons (model DS1922L; Maxim Integrated, San Jose, CA) placed at the surface (covered with a thin layer of sand). Solar radiation incident on a horizontal plane was recorded using a Campbell Scientific CS300 pyranometer (wavelength range 300–1100 nm, measurement range 0–2000 Wm^{-2}). Wind speeds were collected using wind tunnel-calibrated 3-cup micro anemometers on jeweled bearings (Rimco; Rauchfuss Instruments Ltd., Victoria, Australia) with a stall speed of 0.1 m s^{-1} that were placed to record concurrent measurements as close as possible to ground surface (0.12–0.22 m), ~0.5 m, ~1.00 m, and ~2.00 m above the ground. Air temperatures and solar radiation were measured every 60 s, with 15-min averages recorded by the datalogger. Wind speed was measured continuously, with total anemometer rotations recorded at 15-min intervals. The iButtons

sampled temperatures every 15 min. All data were aggregated into hourly averages and the air temperature and wind speed data from various heights were used to calculate the vertical temperature and wind speed profiles at the sites. Relevant inputs to the microclimate submodel are summarized in Table 1.

We evaluated the microclimate model's ability to convert macroclimate weather into microclimate conditions relevant to fiddler crab heat budgets. The microclimate model inputs were the observed hourly macroclimate information (2 m air temperature, wind speed, and relative humidity; solar radiation; cloud cover) and substrate properties including roughness height. We compared predicted and observed surface temperatures, near-ground air temperature and near-ground wind speed using metrics: root mean square error (RMSE), normalized root mean square error (NRMSE, which were normalized to the measured range of values), correlation coefficient (r), and the coefficient of determination (r^2) of a simple linear regression.

2.3. Fiddler crab submodel development

We used a combination of empirical data, 3D modeling software, and computational fluid dynamics software to obtain crab properties needed for NM's ectotherm submodel. The properties needed and the source of the information is summarized in Fig. A.2.

2.3.1. Fiddler crab model properties from empirical data

In the summer of 2019, mass and carapace width were measured from male crabs with intact large claws collected in Panacea, FL, USA (n = 50), Beaufort, NC USA (n = 51), and Stony Brook, NY, USA (n = 50). We used these data to create a regression equation for body weight as a function of carapace width for males with a major (=large) claw (Fig. A.3).

Table 1
Relevant inputs for the microclimate submodel. As described in the text, measured daily minimum and maximum 2m air temperatures and wind speeds were also provided to the model.

Roughness height (m)	0.01–0.03	Calculated from profile of measured near-ground, 0.5m, 1.0 m, and 2 m wind speeds (Fig. A.1)
Surface Reflectivity (%)	42–47	Measured reflectivity for wet and dry sand samples from the three weather station locations.
Soil mineral thermal conductivity (W $m^{-1}{}^{\circ}C^{-1}$)	3.0	Value for quartz from Engineering Toolbox[a]
Soil mineral density (Mg m^{-3})	2.6	Value for quartz from Engineering Toolbox[a]
Soil mineral specific heat (J $kg^{-1}K^{-1}$)	750	Value for quartz from Engineering Toolbox[a]
Soil mineral bulk density (Mg m^{-3})	1.3	Value for sand from Engineering Toolbox[a]
Percent Surface Wet (%)	0–30	Estimation based on observations
Cloud cover (%)	Variable	Calculated based on proportion of measured incoming solar radiation to clear sky incoming radiation.
Maximum Relative Humidity (%)	100	Assumed
Minimum Relative Humidity (%)	Variable	Calculated based on 100% maximum RH and constant water mass in air
Shade (%)	0	Observed
Timing of minimum air temperature and wind speed	Sunrise	Own Estimate
Timing of minimum relative humidity	1 h after solar noon	Own Estimate
Timing of maximum air temperature and wind speed	1 h after solar noon	Own Estimate
Timing of maximum relative humidity	Sunrise	Own Estimate

[a] https://www.engineeringtoolbox.com/.

We measured carapace reflectivity across the 350–2500 nm spectrum using an ASD Field Spectrometer (Fieldspec Pro; Malvern Panalytical, Malvern, United Kingdom) on crabs collected in Beaufort, Panacea and Stonybrook. Because of the variation and plasticity in fiddler crab carapace coloration (Kronstadt et al., 2013), reflectivity measurements were made on a representative selection of crabs on both the light and dark ends of the color spectrum. In order to cover the instrument's field of view with only the dorsal carapace, we arranged four crabs together for both the light and dark measurements.

Metabolic rate as a function of temperature was calculated using a regression of previously-published data for *L. pugilator* under open air conditions (Fig. A.4; Démeusy, 1957; Teal, 1959; Vernberg, 1978). Data were presented in terms of O_2 consumption, and we used a conversion of 19.7 kJ L^{-1} O_2 to convert the reported metabolic rate into watts per gram of body weight.

Evaporative water loss (EWL) rates in *L. pugilator* are a function of the integument's permeability to water and the vapor gradient between the crab's evaporating surface and its environment (Herreid, 1969; Yoder et al., 2007). EWL rate (kg s^{-1} m^{-2}) can be defined as:

$$EWL = \left[\rho_{surf} - (RH \bullet \rho_{air})\right] \times G_w \quad \text{Eq. 2}$$

where ρ_{surf} and ρ_{air} are the saturation water vapor densities (kg m^{-3}) at the animal surface and in the air, respectively; RH is the relative humidity (decimal percent); and G_w is the animal's total body conductance to water loss (m s^{-1}). Conductance is the inverse of the animal's total resistance to water loss (r_{tot}), which has two components: integumental resistance to water loss, r_i, and boundary layer resistance to water loss, r_b:

$$r_{tot} = \frac{\rho_{surf} - (RH \bullet \rho_{air})}{EWL} = r_i + r_b \quad \text{Eq. 3}$$

Boundary layer resistance can be computed from the convective heat transfer coefficient, h_C (W $m^{-2}{}^{\circ}C^{-1}$), using the Chilton-Colburn Analogy (Bird et al., 2002; Riddell et al., 2017):

$$r_b = \frac{\rho \bullet c_p}{h_C \bullet \left[\frac{Pr}{Sc}\right]^{\frac{2}{3}}} \quad \text{Eq. 4}$$

where ρ is density of the air (kg m^{-3}), c_p is the specific heat of the air (J kg^{-1} $^{\circ}C^{-1}$), Pr is the dimensionless Prandtl number and Sc is the dimensionless Schmidt number. These dimensionless numbers are used to simplify the equations and describe properties of the fluid (e.g., air) relevant for heat and mass transfer calculations.

We conducted EWL experiments on live crabs and calculated a regression of integumental resistance as a function of vapor pressure gradient. Crabs were collected from Panacea, FL, USA (Porter Island near Panacea, FL, within the St. Marks National Wildlife Refuge, 30.01559°, −84.36934°). Prior to EWL measurements, crabs were held in room-temperature water baths for 30 min to ensure full hydration, after which they were blotted with a paper towel to remove surface water and weighed to get an initial mass. Crabs were then placed individually in cylindrical desiccation chambers (28-mm diameter × 80 mm long with two inlet ports on one end and two outlet ports on the other; Loligo Systems, Viborg, Germany) within temperature-controlled environmental chambers (I-36VL; Percival Scientific, Perry, IA) for 30–40 min, during which time air was pulled through the desiccation chamber at a constant rate (~7 liters min^{-1}) using a vacuum pump. At the conclusion of the experiment, each crab was removed from the desiccation chamber and T_b was measured internally with a thermocouple probe (Therma Type T High Precision Thermocouple Meters, ThermoWorks, American Fork, UT). The crab was then re-weighed to get a final mass and carapace width was measured. Total EWL was calculated as the difference between initial and final mass measurements.

Air temperature and relative humidity within the environmental chamber were recorded (HOBO U23 Pro v2; Onset Computer Corporation, Bourne, MA) and assumed to be the same as in the desiccation

chamber since air was pulled directly from the environmental chamber into the desiccation chamber. To account for blockage effects, air flow through the desiccation chamber was converted to the wind speed the crabs experienced using the cross-sectional areas of the desiccation chamber and of the crabs, following the principle that the volumetric flow rate of air passing through an imaginary plane normal to the flow in the open tube must equal the volumetric flow rate of air passing through the air portion of an imaginary plane normal to the flow around the largest cross-section of the crab.

EWL measurements were made in three treatment conditions: ~15 °C and 80% relative humidity, ~25 °C and 60% relative humidity, and ~35 °C and 35% relative humidity (n = 10–16 per treatment). Additional EWL measurements at room temperature were taken without collecting T_b using the same experimental design. Finally, we continuously monitored T_b in four individuals in the 15 °C and 35 °C treatments using fine-wire (0.23-mm diameter) thermocouples implanted into the body cavity to check for the magnitude of temperature change taking place between removal from desiccation chamber and temperature measurement.

Total water loss and crab surface area was used to calculate r_{tot}. We used the heat transfer coefficients for fiddler crabs calculated with computational fluid dynamics (described below) and the air properties measured in the environmental chambers to calculate $r_{b.}$ Integumental resistance was calculated as the difference between r_{tot} and r_b.

For crabs in the 15 °C treatment, we used the average T_b of the four continuously-monitored individuals (mean ± SD = 14 ± 0.1 °C) when calculating water loss resistance instead of the final T_b taken from each individual crab. This was a precaution taken because the final T_b measurements of crabs in the 15 °C treatment reflect a rapid warming following their removal from the desiccation chambers rather than body temperatures in the 15 °C chambers, as discussed below.

2.3.2. Fiddler crab model properties from 3D modeling and computational fluid dynamics

We obtained surface areas, silhouette areas and volumes using 3D modeling software. A 3D scan of a dead adult male *L. pugilator* (20.5 mm carapace width), collected from a sand flat in Old Field, Long Island, New York USA (Location: 40.935°, −73.144°) created a triangular mesh that was used to create a non-uniform rational B-spline (NURBS) format virtual fiddler crab using ANSYS Workbench (ANSYS Release 19.0, ANSYS, Inc., Canonsburg, PA) software. The scanned-in model was isometrically scaled up and down between maximum carapace widths of 10–30 mm in 5 mm increments to calculate the surface area and volumes as a function of carapace width (Fig. A.5). From these calculations, regression equations for surface area and volume as a function of maximum carapace width were developed, assuming isometric scaling.

We calculated silhouette area as a function of solar zenith angle in ANSYS SpaceClaim. Planes were created to represent zenith angles in 15° increments from 0° (sun directly overhead) to 90° (sun on the horizon), and we used the measure projected area tool in SpaceClaim to calculate the silhouette area for each angle increment (See example images in Fig. A.6). This was repeated for four orientations: 1) anterior facing the sun; 2) posterior facing the sun; 3) major claw side facing the sun; and 4) minor claw side facing the sun. Regression equations were fitted to the data to develop an equation for silhouette area (expressed as a percent of total surface area) as a function of solar zenith angle (Fig. A.7).

NM calculates animal core-to-surface temperature gradients based on calculations of the combined effects of uniformly distributed internal heat generation within the body flesh coupled with conduction of heat from the core of the animal through the flesh to the surface. The temperature gradient is thus dependent on the shape and distance from the core to the surface. For the purposes of these calculations we approximated the shape of the body as an ellipsoid. The A dimension (side-to-side width) was set to the carapace width; the B dimension (front-to-back width) was set to be ½ of the A dimension and the C dimension (vertical height) was set to be ¾ of the A dimension. These were the approximate relationships of the length, width, and height of the crab body as measured on the 3D crab scan. However, given the crab's small size and low metabolic heat production, the model was not impacted by utilizing this approximation to calculate surface temperatures since there was negligible core-to-surface temperature gradient (see sensitivity analysis results below).

Convective heat transfer coefficients for crabs were calculated by simulating a virtual wind tunnel in ANSYS Workbench following methods detailed in Dudley et al. (2013, 2016). The purpose of these calculations was to calculate baseline whole-body heat transfer coefficients specific to the crab morphology as a function of wind speed at animal height (Kowalski and Mitchell, 1976). This relationship is then used by the animal model to calculate convective heat transfer and, through the Chilton-Colburn Analogy as described above, water mass transfer in any environmental conditions. This procedure is analogous to measuring morphology-specific heat transfer coefficients using metal castings in physical wind tunnels and then using those values for biophysical modeling.

For these calculations we used ANSYS SpaceClaim to create a simplified version of the scanned crab model in order to obtain an acceptable mesh (See Fig. A.8 for a comparison of the scanned model and the simplified model used for heat transfer calculations). We placed the 3D crab model on the floor of a virtual wind tunnel, modeled as a box with a 150 mm buffer to the sides and top, a 50 mm buffer to inlet, and a 250 mm buffer to the outlet. The virtual wind tunnel was imported to ANSYS Meshing and meshed with tetrahedral elements and a 10-layer inflation boundary around the crab (Dudley et al., 2016). With this meshed model, we ran simulations for heat transfer at each wind tunnel speed in ANSYS Fluent. Inlet velocities were set to the wind tunnel velocity and inlet flow was set to low turbulence (1%), consistent with wind tunnel settings traditionally used to derive heat transfer coefficients from metal castings. The outlet was set to zero pressure. The entire surface of the crab model was set to be a uniform 10° warmer than the air temperature (298.15 K) for each simulation. We used the k-ω shear stress transport (SST) model because it provides accurate near-body and free stream performance (Dudley et al., 2016).

Heat transfer coefficients were calculated for five wind speeds (0.1, 1, 4, 5 and 10 m s^{-1}) in order to calculate the Nusselt-Reynolds correlation described below and for four orientations to the wind direction: 1) anterior windward; 2) posterior windward; 3) major claw side windward; and 4) minor claw side windward. Whole-body heat transfer coefficients were calculated in ANSYS CFD Post by integrating heat flux from all surface areas of the crab model. Using these heat transfer coefficients, we calculated the constant and exponent coefficients for a Nusselt (Nu)-Reynolds (Re) correlation (Bird et al., 2002):

$$\mathrm{Nu} = a\mathrm{Re}^{b}, \quad \text{Eq. 5}$$

where

$$\mathrm{Nu} = \frac{h_c L}{k_a} \quad \text{Eq. 6}$$

and

$$\mathrm{Re} = \frac{\rho_a L U}{\mu_a} \quad \text{Eq. 7}$$

where h_c is the heat transfer coefficient (W m^{-2} °C^{-1}), L is the characteristic dimension (m), k_a is the air thermal conductivity (W m^{-1} °C^{-1}), ρ_a is the air density (kg m^{-3}), U is the air speed (m s^{-1}), and μ_a is the air dynamic viscosity (kg m s^{-1}).

Thus, a generalized heat transfer coefficient that the animal model can use for any wind speed or proportional body size can be calculated as:

$$h_c = \frac{k_a}{L} a \left(\frac{\rho_a L U}{\mu_a} \right)^b \quad \text{Eq. 8}$$

The characteristic dimension was taken to be the maximal carapace width, a commonly collected measure of fiddler crab body size and the air properties are known from environmental conditions (air temperature, relative humidity and wind speed). The Nu-Re correlation relates convective heat transfer to the crab's size and morphology and environmental conditions, enabling generalized heat transfer calculations for any size crab in any environmental conditions. Since we do not know wind direction relative to the crab's body orientation at any given moment, we programmed the crab model to use an average heat transfer coefficient from all four orientations.

2.4. Fiddler crab model development: sensitivity analysis

We conducted a sensitivity analysis for the crab model inputs by simulating a crab on the sand surface for an average July day in Beaufort, NC. The microclimate model was parameterized as described above except using 1980–2010 average air temperatures and relative humidities obtained from Climate NA (Wang et al., 2016) and average cloud cover from EarthEnv (Wilson and Jetz, 2016). Individual inputs were varied while holding all other inputs constant to evaluate the effect of input uncertainty on T_b and EWL predictions.

2.5. Biophysical model performance comparison

To evaluate the value of taking the effort to calculate detailed model parameters described above versus using a simpler geometric approximation, we compared T_b and EWL predictions from our full model to an ellipsoidal approximation model.

Two ellipsoidal approximation models were considered. First, an ellipsoid approximating the body exclusive of chelipeds and legs, where the ellipsoid's A-major axis diameter was set to the maximum carapace width. Second, an ellipsoid set to have the same surface area as a fiddler crab (as calculated above in the full model description) and the A-major axis back-calculated using the equation for the surface area of an ellipsoid.

All model parameters for the ellipsoid approximation are the same as for the full model except for heat and mass transfer coefficients, regression for integumental conductance to water loss, volume, and silhouette area (Table 3). The ellipsoidal approximation used the Nusselt-Reynolds correlation for ellipsoids from Clary (1969):

$$\mathrm{Nu} = 0.438 \mathrm{Re}^{0.557} \left(\frac{a}{c} \right)^{-0.07} \left(\frac{b}{c} \right)^{-0.44} \quad \text{Eq. 9}$$

Integumental conductance to water loss as a function of vapor density gradient were calculated as with the full model. Calculations for the ellipsoidal approximation model with the a-major axis set to carapace width required a negative integumental conductance to meet observed whole body water loss rates; thus this model was discarded (but see the body-only model below). Silhouette area as a function of zenith angle and orientation to the sun was calculated as the cross-sectional area of an ellipsoid from Tatum (2022).

Finally, a model of only the body compartment was also developed to test the idea that the legs could be relatively thermally isolated from the body due to lack of sufficient conduction or body fluid flow between the legs and the body. This model was built using the same process as with the full model but excluded appendages from the calculations and applied the whole-animal integumental resistance to water loss from the full model since we do not know the water loss only from the carapace from the experimental procedure.

We compared ability of the different models to accurately predict T_b and EWL by (1) simulating the crabs in the desiccation chamber water loss experiments and (2) simulating crabs in a real beach environment.

When simulating crabs in the desiccation chamber, the microclimate submodel was bypassed and environmental conditions were manually set to the air temperature, wind speed, and relative humidity data collected during the experiments. Incoming solar radiation was set to 0. Separate simulations were run for each experimental crab, setting the model crab's carapace width to the width measured on the experimental crab.

To validate model predictions in a real environment, we compared predicted T_b to observed T_b extracted from thermal images of live crabs on beaches in Panacea and Stonybrook. In Panacea, approximately 10 cm of monofilament line was attached to the crab's carapace and to a small wooden dowel stuck into the sand, tethering the crab in place and preventing the crabs from escaping. In Stonybrook, crabs active on the surface for at least 10 min were opportunistically photographed. Images were taken with a FLIR T360 camera (Teledyne FLIR, Wilsonville, OR; camera calibration was checked against photos of a metal square of known temperature) and crab T_b ($n = 3$ in Panacea and $n = 18$ in Stonybrook) and sand surface temperatures were extracted using FLIR Tools software (Teledyne FLIR; see Fig. A.9 for an example image).

When validating model predictions against these field-observed temperatures, the microclimate model was parameterized with sand surface temperatures from the thermal images, and solar radiation, 2 m air temperatures, wind speeds, and relative humidities collected at the time of the photograph from the weather stations described above. Crabs were simulated in three different combinations of body orientation and carapace absorptivity expected to give maximum, minimum, and average T_b predictions. In the maximum T_b scenario, crabs were simulated in the orientation that maximized silhouette area and with the maximum measured carapace absorptivity. In the minimum T_b scenario, crabs were oriented to minimize silhouette area and the minimum measured carapace absorptivity was used. In the average T_b scenario, the average silhouette area and carapace absorptivity were used.

Crabs photographed in Stonybrook were not handled so body size was unknown. Thus, the minimum, average, and maximum T_b scenarios assumed carapace widths of 16, 18, and 20 mm, respectively. In all scenarios, the crabs were modeled with 35% of their ventral surface in contact with the substrate, based on visual estimations from the live crabs.

2.6. Single site simulation to illustrate use of the biophysical model

To illustrate how biophysical models can provide insight into thermal limitations on fiddler crab distribution and reproductive success, we predict T_b and EWL rates for a fiddler crab (16 mm carapace width; average carapace solar reflectivity) on the surface on an hourly basis over an average year in Beaufort, NC. The microclimate model was parameterized as described for the sensitivity analyses with an additional second run assuming cloudless skies to look at the impact of solar radiation on heat and water balances. We computed the number of hours when the predicted T_b exceed the critical thermal maximum (CT_{max}, approximately 43°C; Darnell and Darnell, 2018; Allen et al., 2012) and the voluntary thermal maximum, the temperature at which crabs seek cooler temperatures (VT_{max}, 33.5 °C; Darnell, unpublished data). We also use the model to explore how body size might affect how long crabs can be on the surface before dehydrating. For this analysis, we performed the same annual simulation described above with a small crab (14 mm carapace width) and a large crab (20 mm carapace width) and used a desiccation threshold of water loss amounting to 10% of total body mass. This level of dehydration has been found to be associated with reduced performance in *L. pugilator* (Allen et al., 2012; Levinton, 2020). For each hour, we use NM's predicted EWL to calculate time to desiccation, based on the model crab's water mass.

3. Results

3.1. Microclimate model validation

Comparisons between predicted and observed surface and near-surface air temperatures are shown in Fig. 1. Predicted temperatures were within 2 °C of observed daytime surface temperatures and within 1 °C of observed daytime near-ground air temperatures across all three sites representing ~5% error from observed (Table 2). Predicted near-ground wind speeds were within 0.3 m s^{-1} from observed, when excluding a brief period of apparently shifted wind direction from the prevailing off-shore direction in Panacea (Fig. 2; Table 2). Across all parameters, r ranged from 0.87 to 0.98, and r^2 ranged from 0.76 to 0.97. All hourly weather station data is available in Appendix B.

3.2. Crab model parameterization results

Crab model parameters are summarized in Table 3. Orienting with the posterior facing the sun tended to create the largest silhouette area while turning sideways to the sun tended to create the smallest silhouette area, with less than 1% difference between the large claw side and the small claw side facing the sun. Orientations with the anterior or posterior facing windward tended to result in greater convective heat transfer compared to orienting sideways to the wind direction (Table 3; Fig. A.10).

EWL measured in the desiccation chambers generally increased with increasing ambient temperatures and vapor pressure deficits, although there was considerable variability between individuals even when comparing similar size and environmental conditions (Fig. 3a and b). EWL increased with increasing vapor pressure deficit in the ambient air (Fig. 3c). All water loss experimental data is available in Appendix B. Total body conductance to water loss decreased with an increasing vapor density gradient between the animal's evaporating surface and the surrounding air (Fig. 4).

3.3. Crab model sensitivity analysis

A sensitivity analysis of animal model inputs indicates that T_b and EWL predictions are most sensitive to carapace solar absorptivity, Nusselt number (Nu), silhouette area and integumental conductance inputs (Fig. A.11). EWL predictions are also sensitive to total surface area. For surface area, solar absorptivity, and silhouette area, there is a positive relationship between the input and T_b and EWL; there is a negative relationship between Nu and T_b and EWL. Integumental conductance is negatively related to T_b and positively related to EWL.

Table 2
Measured and modeled hourly surface temperature and near-surface wind speed and air temperatures compared using root mean square error (RMSE), normalized root mean square error (nRMSE), correlation coefficient (r), coefficient of determination (r^2). Metrics are shown for all observed hours and for only daytime hours.

Parameter	RMSE	nRMSE	r	r^2
Near-surface Wind (all)	0.3	0.14	0.89	0.8
Near-surface Wind (day)	0.3	0.16	0.87	0.76
Surface Temperature (all)	1.7	0.05	0.98	0.95
Surface Temperature (day)	2.1	0.06	0.97	0.95
Near Ground Temperature (all)	0.9	0.04	0.98	0.97
Near Ground Temperature (day)	1	0.05	0.98	0.97

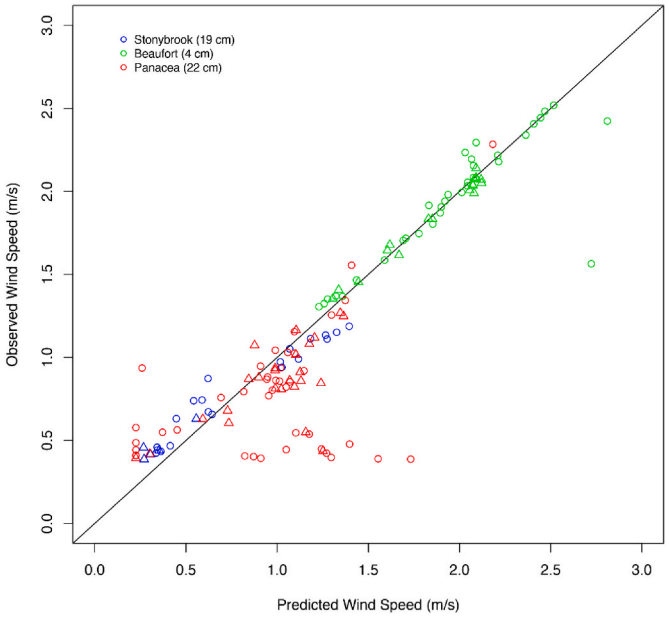

Fig. 2. Predicted and observed near-surface wind speeds in Panacea, FL, Beaufort, NC, and Stonybrook, NY, USA. The microclimate model was parameterized with the values summarized in Table 1 and was provided the observed hourly 2 m wind speeds, air temperatures and incoming solar radiation. This comparison quantifies the model's ability to translate macroclimate data into more biologically-relevant microclimate conditions for fiddler crabs close to the sand surface.

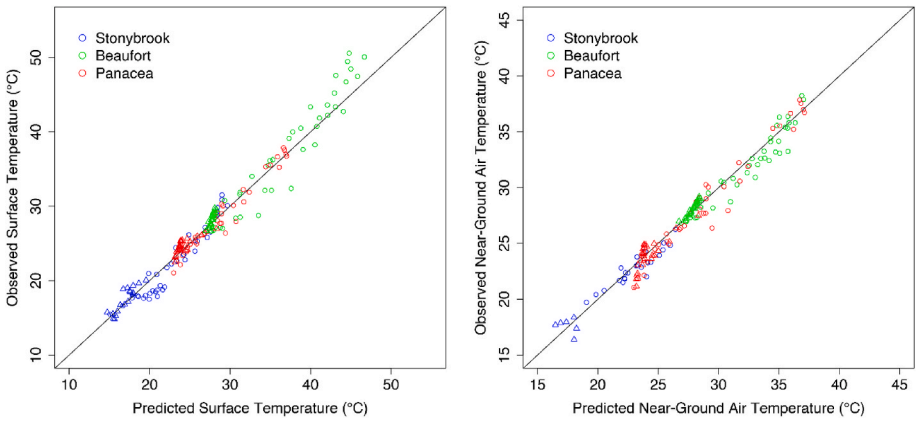

Fig. 1. Predicted and observed surface (a) and near-surface (b) air temperatures in Panacea, FL, Beaufort, NC, and Stonybrook, NY, USA. The microclimate model was parameterized with the values summarized in Table 1 and was provided the observed hourly 2 m wind speeds, air temperatures and incoming solar radiation. This comparison quantifies the model's ability to translate macroclimate data into more biologically-relevant microclimate conditions for fiddler crabs close to the sand surface.

Table 3
Morphological and physiological inputs used to parameterize the fiddler crab biophysical models. In this table, c_w refers to maximum carapace width (mm); T_a refers to air temperature (°C), VDG refers to vapor density gradient (kg m^{-3}), z refers to solar zenith angle (°; 0° is the sun directly overhead; 90° is the sun right on the horizon). For the Nusselt-Reynolds (Nu-Re) correlation coefficients, a and b terms refer to the correlation: $Nu = aRe^b$. Values for the ellipsoidal approximation are presented as percent of the full model to facilitate comparison between the models; detailed equations are presented in Table A1).

Parameter	Full Model	Ellipsoidal Approximation
Body mass (g)	$0.0007c_w^{2.8981}$	Same
Surface area (mm^2)	$8.3118c_w^{1.9929}$	Same
Volume (mm^3)	$0.5304c_w^{2.9891}$	+23%
Metabolic rate (mm^3 O_2 g^{-1} hr^{-1})	$0.1383T_a^2 + 0.5101T_a + 8.707$	Same
Integumental resistance to water loss (s/m)	7899.4(VDG)$^{0.6271}$, with a minimum resistance calculated with VDG = 0.0015 kg m^{-3} and a maximum resistance calculated with VDG = 0.0219 kg m^{-3}	−22% (minimum VDG) to −3% (maximum VDG)
Carapace absorptivity (dec. pct.)	0.85 (light) – 0.88 (dark)	Same
Silhouette area (% surface area) (Anterior facing sun)	$5.54721E\text{-}9z^4$-$4.73882E\text{-}7z^3$-$1.62394E\text{-}5z^2$+$1.21856E\text{-}3z$+0.20894	+41% (75° zenith angle) to +7% (0° zenith angle)
Silhouette area (% surface area) (Posterior facing sun)	$1.45081E\text{-}8z^4$-$2.97380E\text{-}6z^3$+$1.79321E\text{-}4z^2$+$2.66127E\text{-}3z$+0.20898	
Silhouette area (% surface area) (Large claw side facing sun)	$-9.70499E\text{-}6z^2$-$3.40430E\text{-}4z$+0.21168	
Silhouette area (% surface area) (Small claw side facing sun)	$-7.98788E\text{-}6z^2$-$4.74417E\text{-}4z$+0.21088	
Nu-Re correlation terms (Anterior windward)	$Nu = 0.99Re^{0.50}$*	−38% (Re = 125) −15% (Re = 10,000)
Nu-Re correlation terms (Posterior facing sun)	$Nu = 0.94Re^{0.51}$*	
Nu-Re correlation terms (Large claw side windward)	$Nu = 1.44Re^{0.48}$*	
Nu-Re correlation terms (Small claw side windward)	$Nu = 1.40Re^{0.45}$*	

*Calculated for 127<Re < 12,761

3.4. Ellipsoidal approximation parameter comparison

The ellipsoidal approximation model had a lower heat transfer coefficient than the full model (Fig. A.12). This translated into a lower boundary layer conductance to water loss and, consequently a 6% (35 °C treatment) to 30% (15 °C treatment) higher integumental conductance to water loss (Fig. 4). Average silhouette area for the ellipsoidal approximation was larger, ranging from 48% larger than the average full model silhouette area at a zenith angle of 75° to 7% larger at a zenith angle of 0° (the sun directly overhead) (Fig. A.13).

3.5. Crab model performance comparison

When simulating crabs in the desiccation chamber water loss experiments, the full model predicted T_b to within 1 °C of observed for crabs in the 25 °C and 35 °C treatments (Fig. 5a; RMSE = 1.0 °C, NRMSE = 0.09, r = 0.98, R^2 = 0.96). The ellipsoidal approximation predicted T_b to within 1.6 °C for the same crabs (Fig. 5b; RMSE = 1.6 °C, NRMSE = 0.14, r = 0.98, R^2 = 0.97). The internal measurements of crabs in the 15 °C treatment likely reflect the rapid warming of the crabs following handling and removal from the environmental chamber prior to temperature measurements since they are implausibly higher than the treatment temperature of 15 °C and the continuous temperature monitoring indicates that crabs in the chamber maintain a lower T_b (Fig. 5). The full model's predicted T_b for the 15 °C treatment crabs with continuous temperature monitoring was 0.2 ± 0.1 °C cooler than the measured T_b. The ellipsoidal model's predicted T_b for the 15 °C treatment crabs with continuous temperature monitoring was 0.6 ± 0.1 °C cooler than the measured T_b. Similarly, the 35 °C treatment temperature measurements may have been influenced by the crabs quickly cooling toward room temperature after being removed from the chambers prior to measurement. Continuous temperature monitoring of crabs in the desiccation chamber indicate a higher temperature than measured on some of the 35 °C treatment crabs (Fig. 5). The full model's predicted T_b for the 35 °C treatment crabs with continuous temperature monitoring deviated by 0.4 ± 0.4 °C from the measured T_b. The ellipsoidal approximation's predicted T_b deviated by 2.2 ± 0.4 °C from the measured T_b.

The full model's EWL predictions are strongly correlated with measured EWL and lay in the middle of the range of measured values for all treatments (Fig. 6a; RMSE = 1.77E-5 g s^{-1}, nRMSE = 0.17, r = 0.81, R^2 = 0.66). The ellipsoidal approximation performed similarly (Fig. 6b; RMSE = 2.2E-5 g s^{-1}, NRMSE = 0.21, r = 0.81, R^2 = 0.66).

When simulating crabs with IR photographs in a real world environment, the full model, using average silhouette area, body size, and

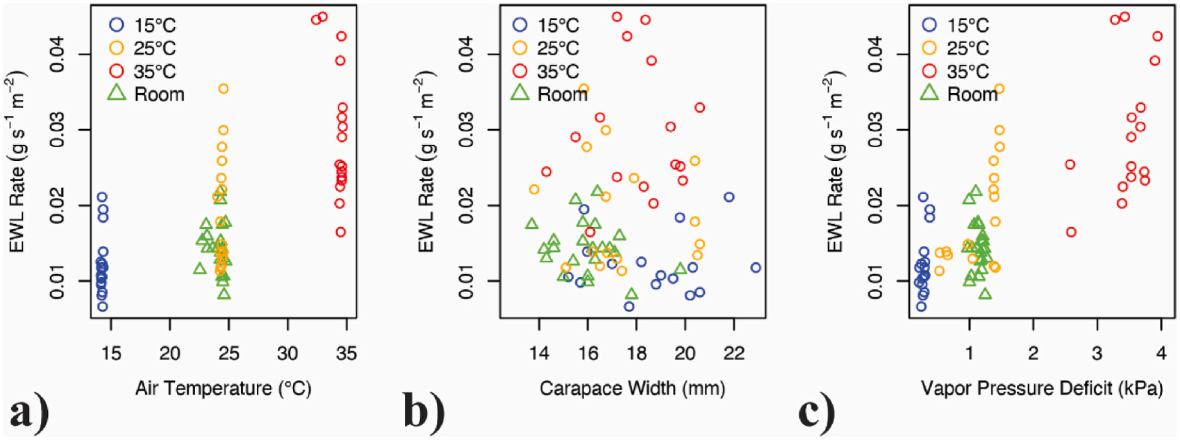

Fig. 3. Experimental evaporative water loss (EWL) data as a function of ambient temperature (a), carapace width (b), and vapor pressure deficit in the ambient air (c) from male crabs placed in desiccation chambers at 15 °C/80% relative humidity, 25 °C/60% relative humidity or 35 °C/30% relative humidity. Additional EWL measurements were taken at room temperature (22.5–24.7 °C; 56–82% relative humidity) without measuring body temperature.

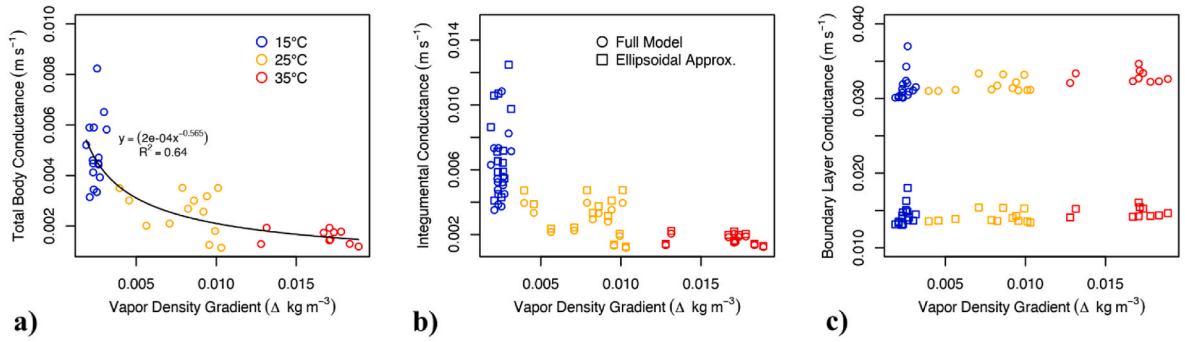

Fig. 4. Measured total conductance to water loss as a function of vapor density gradient (a) and calculated integumental (b) and boundary layer conductance (c) as a function of vapor density gradient. Calculations for the full crab model are represented by circles and calculations for the ellipsoidal approximation are represented by squares. The reduced total body conductance to water loss with increasing vapor density gradient is driven by reduced integumental conductance at higher vapor density gradients.

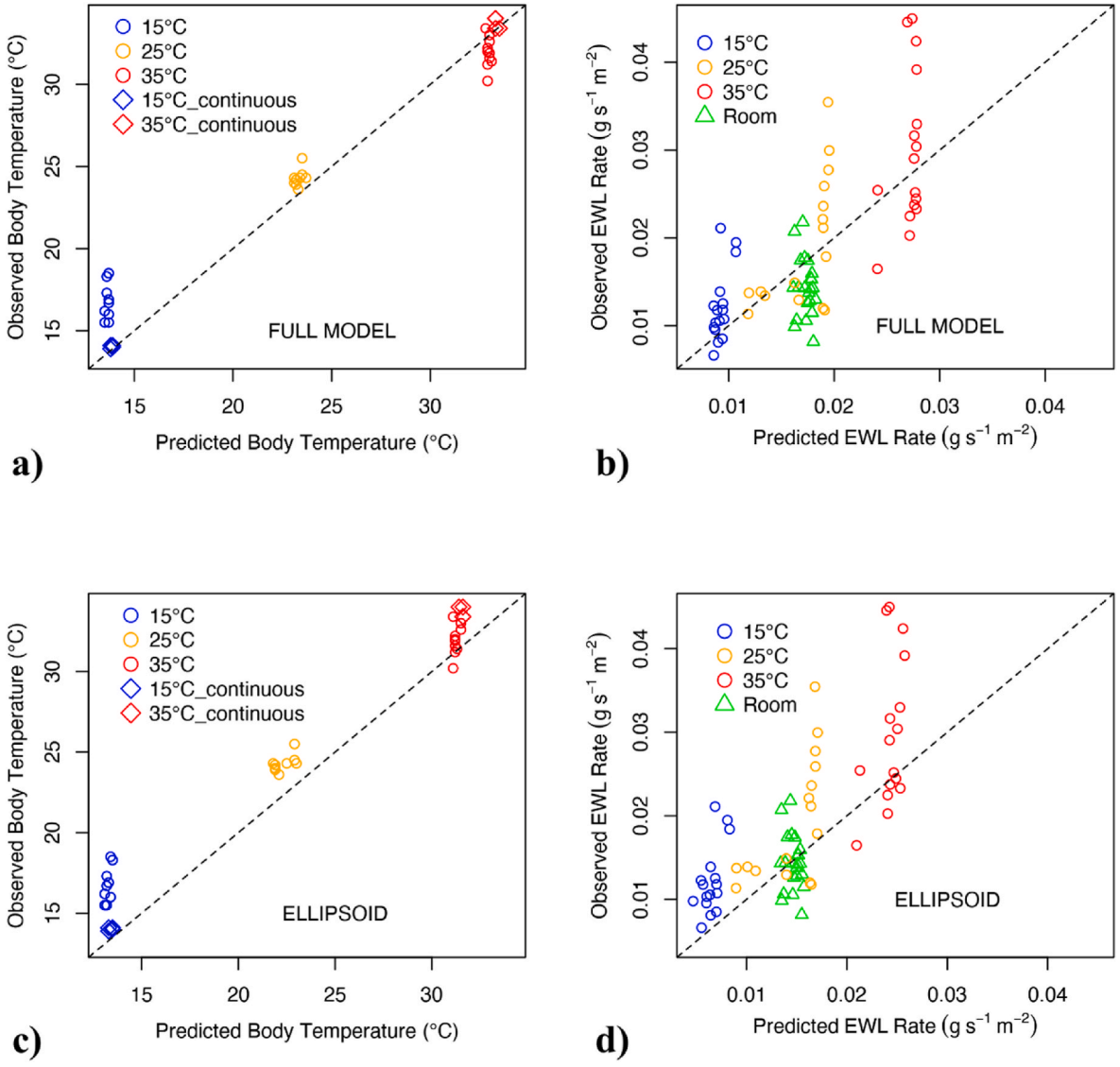

Fig. 5. Predicted crab body temperatures (T_b) compared to measured T_b for the full model (a) and ellipsoidal approximation model (c) and predicted evaporative water loss (EWL) compared to measured EWL for the full model (b) and ellipsoidal approximation model (d) for crabs in the desiccation chamber water loss experiments. T_b were measured with an internal probe after being removed from the desiccation chamber. Continuous T_b measurements were also taken for four crabs in the 15 °C and 35 °C treatments and final steady state T_b from these individuals are shown. Additional EWL measurements were taken at room temperature (22.5–24.7 °C; 56–82% relative humidity). The solid lines indicate a 1:1 match.

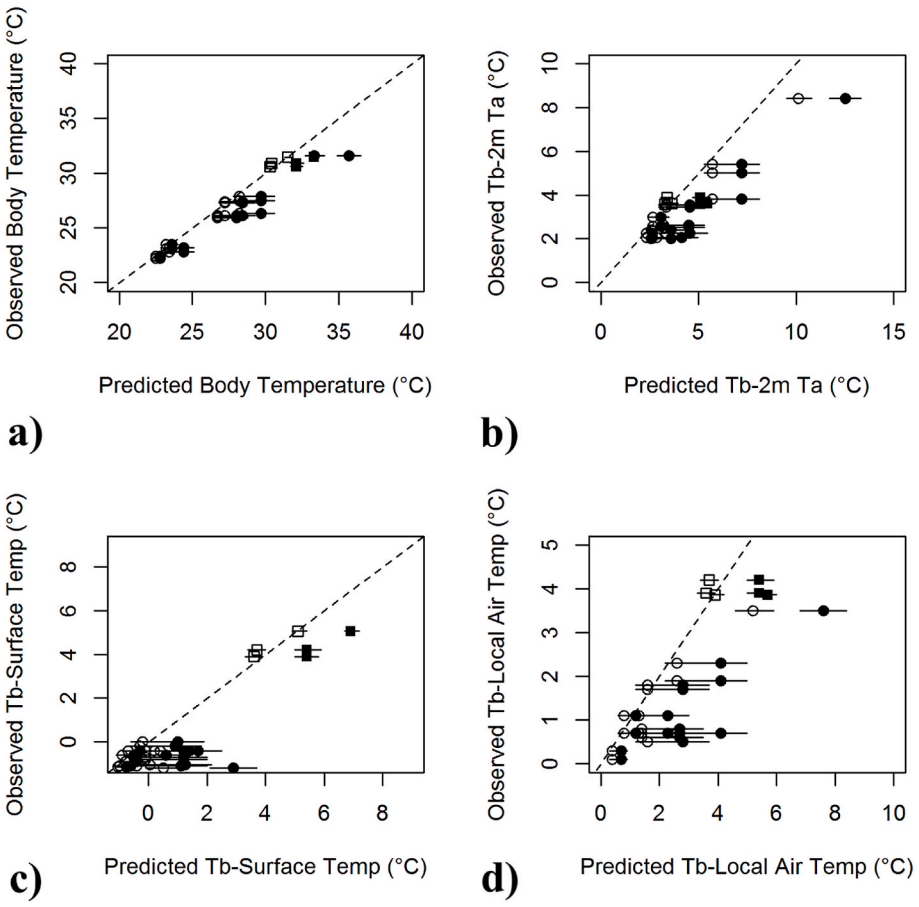

Fig. 6. Predicted and measured body temperatures (T_b) of male fiddler crabs on the sand surface in Stonybrook, NY, USA (circles) and Panacea, FL, USA (squares). T_b are also shown as differences from 2m air temperature (b), sand surface temperature (c), and air temperature at animal height (1.75 cm; d). Open symbols are predictions from the full model and closed symbols are predictions from the ellipsoidal approximation model. The horizontal lines indicate range of model predictions: the maximum predicted temperature assumes maximum surface area directly exposed to the sun and minimum carapace solar reflectivity; the minimum predicted temperature assumes minimum surface area directly exposed to the sun and maximum carapace solar reflectivity. The average prediction assumes an average surface area directly exposed to the sun and an average carapace solar reflectivity.

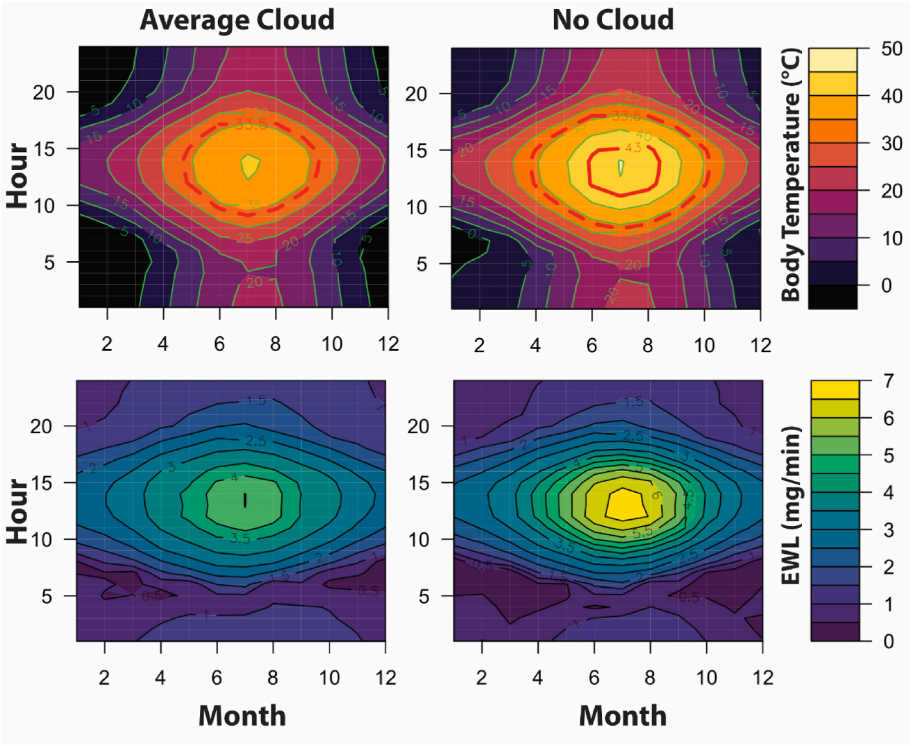

Fig. 7. Annual hourly predicted body temperature and evaporative water loss (EWL) rates for a male fiddler crab on the surface in Beaufort, NC, USA under average cloud conditions and under cloudless conditions. The solid red contour indicates hours when the T_b exceeds a critical thermal maximum temperature (43 °C); the dashed red contour indicates hours when the T_b exceeds the voluntary maximum thermal temperature (33.5 °C). These hours are indicative of extreme and moderate heat stress, respectively, when crabs would be expected to retreat to burrows more frequently for thermoregulation. For ecological context, the breeding season peaks in the summer months (and extends from ~April to ~September). (For interpretation of the references to color in this figure legend, the reader is referred to the Web version of this article.)

carapace reflectivity inputs predicted T_b within 0.7 °C for surface-active crabs on beaches in Panacea, FL and Stonybrook, NY (Fig. 6; RMSE = 0.72 °C, NRMSE = 0.08, r = 0.98, R^2 = 0.96). Predictions when using heat-gain-minimizing inputs for silhouette area, body size and carapace reflectivity were closer to observed T_b (Fig. 6; RMSE = 0.58 °C, NRMSE = 0.06). The ellipsoidal approximation, using average silhouette areas, body size, and carapace reflectivity inputs predicted T_b within 2.0 °C (Fig. 6; RMSE = 1.8 °C, NRMSE = 0.19, r = 0.98, R^2 = 0.95).

3.6. Illustrative single site simulation

Under average cloud cover in Beaufort, NC, T_b are not predicted to exceed CT_{max} at any point during the year; under cloudless conditions CT_{max} would be exceeded for up to 5 h a day in July, indicating that frequent retreats to burrows would be required (Fig. 7). VT_{max} was exceeded by up to 8 h a day under average cloud cover and up to 10 h a day under cloudless conditions. Using the predicted EWL rates (Fig. 7), time to desiccation (using a threshold of 10% water loss) was as fast as 48 min in July under average cloud cover and 32 min in July under cloudless conditions. Time to desiccation depends on body size with larger crabs taking longer to dehydrate (Fig. 8). Maximum predicted desiccation time under cloudless conditions for a small crab was 29 min compared to 38 min for a large crab.

4. Discussion

This work illustrates the importance of using accurate species-specific morphology and heat and mass transfer properties in biophysical models used to predict body temperatures (T_b) and evaporative water loss (EWL). We utilized a combination of empirical measurements, 3D modeling and CFD to create and test a detailed biophysical model for an animal with a very complex geometry. The 3D modeling and CFD enabled us to get accurate measurements of parameters like surface and silhouette areas and convective heat transfer coefficients that would be otherwise be very difficult to measure on animals with such a complex geometry. As the sensitivity analyses show, these inputs are primary drivers of model predictions, demonstrating the importance of accurate values for these parameters.

Similarly, the simultaneous laboratory measurements of both EWL and T_b were critical to the model development and validation since T_b is dependent on EWL rates (and vice versa). This combination of methodologies allows us to provide an improvement upon a prior *L. pugilator* biophysical model (Smith and Miller, 1973) by incorporating variable water permeability as a function of environmental condition as observed in live crabs, providing more accurate calculations of surface and silhouette areas, and demonstrating simultaneous validation of predicted T_b and EWL rates over a range of environmental conditions.

This full, detailed model more accurately predicted T_b in live crabs than did a simpler ellipsoidal approximation even when the ellipsoidal approximation is provided with an accurate surface area. Importantly, the improvement can be more than 2 °C closer to observed T_b under simulated real world conditions. This is a biologically-relevant improvement that can impact interpretations of, and confidence in, model predictions of thermal stress (c.f., Bakken and Angilletta, 2014). This improved accuracy is particularly important when dealing with species with narrow thermal margins of safety between optimal and maximum critical temperatures, who are most vulnerable to climate change and thus make good candidates for modeling analyses (Deutsch et al., 2008).

A detailed look at individual heat fluxes from the two modeling approaches when assuming the observed body temperature illustrates how model predictions differed (Table 4). For a simulation of a crab on the beach in Panacea, FL where solar input creates T_b higher than surrounding air temperature, the ellipsoidal approximation's lower heat transfer coefficient predicted too little convective heat loss to help offset solar heat gain and balance the heat budget. Thus, this model needed a higher T_b (33.3 °C) to generate enough convective heat loss to satisfy the heat balance. The zenith angle for this simulation (15°) meant that there was only ~5% difference in silhouette area between the models. However, a simulation at a lower zenith angle where there is more silhouette area deviation would exacerbate the difference between the models due to the ellipsoidal approximation modeling proportionally more solar heat gain at lower zenith angles, which would need an even higher T_b to generate enough convective heat loss to offset.

For a simulation of a crab in the 35 °C desiccation chamber, there was no solar input and so T_b were below air temperature due to the crab's evaporating surface. Here, the ellipsoidal approximation's lower heat transfer coefficient resulted in not enough convective heat gain to offset heat loss from evaporation. Thus, this model needed a lower T_b (31.6 °C) to obtain enough convective heat gain satisfy the heat balance.

These two examples illustrate how simple geometric approximations may be sufficient in situations where the model organism's body temperature is at or near local air temperatures. However, as body temperature deviates from air temperature, erroneous heat transfer coefficients will begin resulting in unreliable body temperatures. Here we have provided the simple geometric approximation with the correct surface area, but errors in total surface area will impact all heat fluxes (other than metabolic heat production) and silhouette area error will impact solar heat flux.

Comparing the full model to an ellipsoidal approximation also highlights a conundrum faced by biophysical modelers when accurate morphological and heat transfer properties are not available. A modeler can conserve surface area to get full environmental heat and mass fluxes, which are dependent on surface area. However, this comes with the

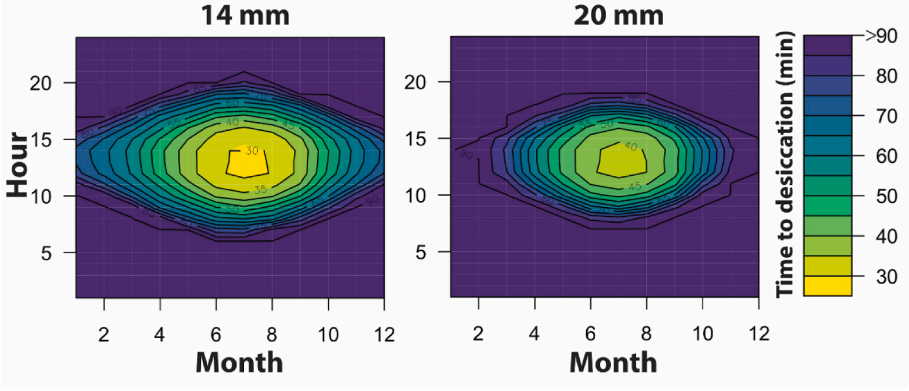

Fig. 8. Annual hourly predicted time to desiccation for a small (14 mm carapace width) and large (20 mm carapace width) male fiddler crab on the surface in Beaufort, NC, USA under cloudless conditions. Time to desiccation is calculated based on desiccation stress affecting performance when water loss amounts to 10% of total body mass (Allen et al., 2012).

Table 4
Individual heat flux breakdown between full model and the ellipsoidal approximation when assuming the observed crab body temperature for both models to illustrate the model differences. All units are watts; $Q_{ir,net}$ is $Q_{ir,in}$-$Q_{ir,out}$. The observed body temperature (T_b) was 31.5 °C on the beach and 33.4 °C in the desiccation chamber. The full model's final predicted T_b that satisfied the heat balance were 31.5 °C on the beach and 33.3 °C in the desiccation chamber. The ellipsoidal approximation's T_b that satisfied the heat balance were 33.3 °C on the beach and 31.6 °C in the desiccation chamber.

		Q_{solar}	$Q_{ir,net}$	Q_{metab}	Q_{evap}	Q_{conv}	Q_{cond}	Heat Balance
Beach	Full Model	0.473	−0.101	0.002	0.082	0.178	0.108	0.007
	Ellipsoidal Approximation	0.495	−0.101	0.002	0.080	0.084	0.108	0.123
Desiccation Chamber (35 °C treatment)	Full Model	0.000	0.021	0.002	0.142	−0.103	−0.001	−0.023
	Ellipsoidal Approximation	0.000	0.021	0.002	0.139	−0.045	−0.001	−0.070

understanding (or even unwittingly if not paying attention to the effect of morphological choices on the model) that the resulting morphology may lead to low convective heat/mass transfer and inflated solar heat gain.

Alternatively, one can model only a portion of the body that is more readily approximated by a simple geometry, like only the body compartment of the fiddler crab. However, the most biologically-relevant aspect of water loss is whole body water loss since it determines dehydration levels rather than a rate. Thus, it is important to be able to model water loss from the entire body surface. When approximating just the body compartment as an ellipsoid, a biologically-implausible negative resistance to water loss was required to match the observed water loss due to evaporative water loss in live crabs occurring not just from the body compartment. Even if one had access to water loss from only a subset of the body and could build a model with a realistic integumental resistance, it is still limited. As illustrated by our body-only model (which is roughly equivalent to a body-only ellipsoidal approximation), T_b may be better predicted than using the surface-area-conserving approximation but the body-only model substantially underestimates total water loss (Figs. A.14, A.15) and thus has limited value in evaluating whole animal hydric stress. This is an important limitation, given the increasing appreciation of, and interest in modeling of, the role of hydric stress as a limiting factor in animal fitness currently and into the future with climate change.

In contrast, the 3D modeling/CFD approach we are highlighting here allows for a model to integrate the whole-body heat and mass properties of a complex anatomy without having to make such compromises. Furthermore, using 3D modeling and CFD software may represent a more accessible and practical means for biophysical modelers to obtain these important parameters than the traditional process of putting metal castings into physical wind tunnels. Previously-published methodologies (e.g., Dudley et al., 2013, 2016) can help to clear the initial hurdle of becoming familiar with the software. Once the initial learning curve is cleared, this approach can facilitate explorations of heat transfer properties for many different body plans and postures without the need for printing individual metal castings and the physical space needed to maintain a wind tunnel.

The microclimate submodel validation also demonstrates how NM can accurately simulate hourly microclimate conditions in the fiddler crab's habitat. This re-confirms prior validations in sandy beach habitats from Fuentes and Porter (2013) and Bentley et al. (2020). The thermal environment for many small species is dominated by surface-level conditions rather than 2 m or 10 m conditions, which is the height where most spatial temperature data is measured and reported. Thus, having a model that can convert macroclimate data into microclimate data more biologically-relevant to animal heat exchange is valuable.

4.1. Limitations

This work demonstrates how incorporating species-specific morphological properties into can improve biophysical modeling accuracy compared to using simpler geometric approximations. However, the model still does have limitations. The full model aggregated the whole body into one representative model shape that incorporates the impact of the claws and legs on total body surface area, silhouette area, and convective heat transfer coefficient. This approach assumes uniform surface temperatures and heat and mass transfer across all surface areas. In turn, this assumes uniform heating of all parts or sufficient heat transfer between all body parts to ensure homogenous heat distribution, which may or may not be the case. For example, the relatively high heat transfer rate of the legs is incorporated into the whole-body heat transfer coefficient, but the legs could be relatively thermally isolated from the body due to lack of sufficient conduction or body fluid flow between the legs and the body. Similarly, a whole body water loss rate was calculated, integrating water loss from all body parts, but in reality there are likely differences in permeability to water loss in different parts of the body such as reduced water loss in the thicker major claw compared to the carapace (Levinton, 2020).

The body-only model has a heat transfer coefficient ~10–20% lower than the full model (Figure A.12). When evaluating performance against field-measured body temperatures, the body-only model performance, although representing an improvement over the surface-area-conserving ellipsoidal approximation, was still worse than the full model (Figure A.15; 1.13 °C RMSE vs 0.72 °C RMSE for the full model; 12% error vs. 8% error for the full model). This suggests that the body temperature is indeed modified by the presence of the appendages, justifying our whole-animal approach. Furthermore, under simulations of more stressful conditions—which are likely of most interest to modelers—the body-only model deviated further away from the full model predictions (Fig. A.16).

This single-shape aggregation was a simplifying assumption we made that still provides better predictions than an even simpler geometric approximation (i.e., the ellipsoid approximation model), but we recognize an even more accurate model would model heat and water fluxes from the body, the claws and the legs separately and explicitly account for heat exchange within and between all the different body parts. This is beyond the scope of the current modeling but could perhaps be accomplished via an approach such as finite element analysis.

Our convective heat transfer coefficients were calculated in a low-turbulence virtual wind tunnel, but real-world conditions can include turbulent air flow, which will increase heat transfer coefficients by scrubbing away boundary layers (e.g., Kowalski and Mitchell, 1976). Use of our calculated heat transfer coefficients in real world simulations could be underestimating convective heat loss should the crabs be affected by turbulent air flow (see Fig. A.11 for sensitivity analysis of 20% and 100% enhancement of Nusselt number). However, our calculated roughness heights of 1–3 cm suggests that small fiddler crabs are largely existing in a laminar sublayer beneath any turbulent flow. Indeed, the Re numbers calculated in local conditions for the simulations of the IR-photographed crabs are less than 1000, well below the Re numbers of the transition from laminar to turbulent flow (~2000–4000).

A better understanding of water loss mechanisms in the crabs would also improve biophysical model since T_b is influenced by water loss rates. The available information that we are aware of (Herreid, 1969; Yoder et al., 2007; Levinton, 2020) provides some good, broad foundational information, but more detailed investigation is needed for a

complete understanding. Namely, there was substantial variation of up to over two-fold difference in EWL rates observed for crabs of similar size in similar environmental conditions, as has been previously reported (Levinton et al., 2015). Within a given treatment in the EWL experiments, crabs with higher T_b had lower EWL rates. However, without incorporating a mechanism for inter-crab variability in water loss rates, the model assumes that two crabs of the same size in the same environmental conditions would have the same EWL rate and thus have the same T_b. The reason for the wide intra-crab variability is unclear but may be related to differences in integument permeability to EWL.

There is also potentially some physiological control of EWL in fiddler crabs that could vary by individual, as evidenced by the increased integumental resistance to water loss with increasing vapor density gradient observed in the laboratory experiments. We examined videos of crabs in the desiccation chambers and did not observe any postural changes that would reduce surface area available for EWL (and thus reduce total EWL) in the warmer in the warmer and drier treatments. The lack of behavioral explanation points to physiological control similar to that previously reported in salamanders (Riddell and Sears 2015; Riddell et al., 2019). Alternatively, this could reflect a physical process as an increased resistance as the exoskeleton dries out in warmer and drier conditions. Additional research would be needed to confirm this in a larger sample size and identify the exact mechanism for the observed trend. Additional research should also investigate population-level differences in integumental resistance to water loss and potential control over the resistance.

Finally, an understanding of how long it takes crabs to cool off and rehydrate in their burrows is necessary to develop a complete understanding of the ecological and reproductive impacts of thermal and hydric stress predicted for surface-active crabs. This model can quantify the thermal and hydric stress the crabs will experience on the sand surface in a given environment; however, how much this stress will limit surface activity is dependent on how fast crabs can recover from different levels of stress upon retreating to their burrow.

5. Conclusions

Biophysical modeling allows mechanistic connections to be established that tie local microclimate conditions and a species' morphology and physiology to feasible behaviors, their durations, and, ultimately, potential fitness consequences. This is critical for understanding species' responses to climate change. However, to provide useful outputs, models need to use the best available inputs. As we illustrate here, taking the effort to get species-specific total surface areas, silhouette areas, and heat and mass transfer properties produces biologically-meaningful improvements compared to relying on simple geometric approximations.

Fiddler crabs provide an excellent model framework due to the stressful environment they operate in, but such mechanistic insights that can be gained from biophysical models are applicable to any other species subject to thermal or hydric stress. The simulations over an average year in Beaufort provides an example of the analyses that are possible with a biophysical model. Similar simulations can be conducted at a landscape scale to evaluate how thermal stress varies across the *L. pugilator*'s distribution. Using biophysical models also allows such landscape analyses to incorporate any known or suspected gradients in morphology or physiology (e.g., Darnell and Darnell, 2018) by explicitly including such characteristics as inputs into the model.

We illustrate here the impact of cloud cover on thermal and hydric stress, but other microclimate variables such as vegetative shading or substrate characteristics could be altered to investigate the importance of microhabitat heterogeneity in providing thermal refuge. Finally, future climate scenarios can be simulated in the microclimate submodel in order to explore potential increases in thermal and hydric stress across the species' range to see what populations might be most impacted by global warming (e.g. Mathewson et al., 2017).

Funding

This work was supported by the National Science Foundation under Grant IOS-1755389. Any opinions, findings, and conclusions or recommendations expressed in this material are those of the authors and do not necessarily reflect the views of the National Science Foundation.

CRediT authorship contribution statement

Paul D. Mathewson: Conceptualization, Methodology, Formal analysis, Software, Investigation, Data curation, Writing – original draft, Visualization. **M. Zachary Darnell:** Methodology, Data curation, Investigation, Resources, Writing – review & editing, Supervision, Funding acquisition. **Zachary M. Lane:** Methodology, Investigation, Writing – review & editing. **Talene G. Yeghissian:** Methodology, Investigation, Writing – review & editing. **Jeffrey Levinton:** Conceptualization, Resources, Investigation, Writing – review & editing, Funding acquisition. **Warren P. Porter:** Conceptualization, Methodology, Software, Formal analysis, Investigation, Visualization, Supervision, Resources, Writing – review & editing, Funding acquisition.

Declaration of competing interest

The authors declare the following financial interests/personal relationships which may be considered as potential competing interests: Warren P. Porter is founder and CEO of Niche Mapper, LLC.

Acknowledgements

We thank David Lovelace (UW-Madison Geology Museum) and Ke Li (UW-Madison, Wisconsin Institute of Medical Research) for assistance with the 3D scanning. Megan Fitzpatrick assisted with the 3D modeling and computational fluid dynamics. Fariba Assadi-Porter and Candice Sheehan provided valuable assistance collecting field data. Dan Rittschof kindly provided laboratory space at the Duke University Marine Lab. We thank Stephen Abrams for providing access and equipment to assist data collection at Flax Pond Marine Laboratory in Stonybrook. Finally, we thank two anonymous reviewers for insightful comments, suggestions and critiques that have greatly improved this work.

Appendix A. Supplementary data

Supplementary data to this article can be found online at https://doi.org/10.1016/j.jtherbio.2023.103613.

References

Allen, B., Rodgers, B., Tuan, Y., Levinton, J.S., 2012. Size-dependent temperature and desiccation constraints on performance capacity: implications for sexual selection in a fiddler crab. J. Exp. Mar. Biol. Ecol. 438, 93–99.
Allen, B.J., Levinton, J.S., 2014. Sexual selection and the physiological consequences of habitat choice by a fiddler crab. Oecologia 176, 25–34.
Bakken, G.S., Angilletta, M.J., 2014. How to avoid errors when quantifying thermal environments. Funct. Ecol. 28, 96–107.
Bentley, B.P., Kearney, M.R., Whiting, S.D., Mitchell, N.J., 2020. Microclimate modelling of beach sand temperatures reveals high spatial and temporal variation at sea turtle rookeries. J. Therm. Biol. 88, 102522.
Bird, R.B., Stewart, W.E., Lightfoot, E.N., 2002. Transport Phenomoena, second ed. John Wiley & Sons, New York.
Briscoe, N., Morris, S., Buckley, L., Mathewson, P., Jusup, M., Levy, O., Maclean, I., Pincebourde, S., Riddell, E., Roberts, J., Schouten, R., Sears, M., Kearney, M., 2023. Mechanistic forecasts of species response to climate change: the promise of biophysical ecology. Global Change Biol. 29, 1451–1470.
Cahill, A.E., Aiello-Lammens, M.E., Fisher-Reid, M.C., et al., 2013. How does climate change cause extinction? P. Roy. Soc. B 280, 20121890.
Christy, J.H., 1982a. Burrow structure and use in the sand fiddler crab, *Uca Pugilator* (Bosc). Anim. Behav. 30, 687–694.
Christy, J.H., 1982b. Adaptive significance of semilunar cycles of larval release in fiddler crabs (genus Uca): test of a hypothesis. Biol. Bull. 163, 251–263.
Clary, B.L., 1969. Convective Heat Transfer Coefficients from Ellipsoidal Models and Irregular Shapes to Air. PhD Thesis. Oklahoma State University, Stillwater, OK, USA.

Crane, J., 1975. Fiddler Crabs of the World (Ocypodidae: Genus *Uca*). Princeton University Press, Princeton.
Darnell, M.Z., Darnell, K.M., 2018. Geographic variation in thermal tolerance and morphology in a fiddler crab sister-species pair. Mar. Biol. 165, 26.
Darnell, M.Z., Yeghissian, T.G., Lane, Z.M., 2020. Balancing risk and reward: mating opportunity influences thermal refuge use in fiddler crabs. Anim. Behav. 169, 51–56.
Démeusy, N., 1957. Respiratory metabolism of the fiddler crab *Uca pugilator* from two different latitudinal populations. Biol. Bull. 113, 245–253.
Deutsch, C.A., Tewksbury, J.J., Huey, R.B., Sheldon, K.S., Ghalambor, C.K., Haak, D.C., Martin, P.R., 2008. Impacts of climate warming on terrestrial ectotherms across latitude. P. Natl. Acad. Sci. USA 105, 6668–6672.
Dudley, P.N., Bonazza, R., Porter, W.P., 2013. Consider a non-spherical elephant: computational fluid dynamics simulations of heat transfer coefficients and drag verified using wind tunnel experiments. J. Exp. Zool. 319A, 319–327.
Dudley, P.N., Bonazza, R., Porter, W.P., 2016. Climate change impacts on nesting and interesting leatherback sea turtles using 3D animated computational fluid dynamics and finite volume heat transfer. Ecol. Model. 320, 231–240.
Fitzpatrick, M.J., Zuckerberg, B., Pauli, J.N., Kearney, M.R., Thompson, K.L., Werner II, L.C., Porter, W.P., 2019. Modeling the distribution of niche space and risk for a freeze-tolerant ectotherm, *Lithobates sylvaticus*. Ecosphere 10, e02788.
Fitzpatrick, M.J., Porter, W.P., Pauli, J.N., Kearney, M.R., Notaro, M., Zuckerberg, B., 2020. Future winters present a complex energetic landscape of decreased costs and reduced risk for a freeze-tolerant amphibian, the Wood Frog (*Lithobates sylvaticus*). Global Change Biol. 26 https://doi.org/10.1111/gcb.15321, 6350-6262.
Fuentes, M., Porter, W.P., 2013. A new approach to model soil temperature: using microclimate models to predict the impacts of climate change on sea turtles. Ecol. Model. 251, 150–157.
Herreid, C.F., 1969. Integument permeability of crabs and adaptation to land. Comp. Biochem. Physiol. 29, 423–429.
Huang, S.-P., Porter, W.P., Tu, M.-C., Chiou, C.-R., 2014. Forest cover reduces thermally suitable habitats and affects responses to a warmer climate predicted in a high-elevation lizard. Oecologia 175, 25–35.
Hyatt, G.W., Salmon, M., 1978. Combat in the fiddler crabs Uca pugilator and U. pugnax: a quantitative analysis. Behaviour 65, 182–211.
Kearney, M., Phillips, B.L., Tracy, C.R., Christian, K.A., Betts, G., Porter, W.P., 2008. Modelling species distributions without using species distributions: the cane toad in Australia under current and future climates. Ecography 31, 423–434.
Kearney, M., Porter, W.P., 2009. Mechanistic niche modelling: combining physiological and spatial data to predict species' ranges. Ecol. Lett. 12, 334–350.
Kearney, M., Porter, W.P., 2017. NicheMapR – a R Package for biophysical modelling: the microclimate model. Ecography 40, 664–674.
Kearney, M., Porter, W.P., 2020. NicheMapR – an R package for biophysical modelling: the ectotherm and dynamic energy budget models. Ecography 43, 85–96.
Kearney, M.R., Munns, S.L., Moore, D., Malishev, M., Bull, C.M., 2018. Field tests of a general ectotherm model show how water can limit lizard activity and distribution. Ecol. Monogr. 88, 672–693.
Kowalski, G.J., Mitchell, J.W., 1976. Heat transfer from spheres in the naturally turbulent, outdoor environment. Amerc. Soc. Mech. Eng. J. Heat Transfer 98, 649–653.
Kronstadt, S.M., Darnell, M.Z., Munguia, P., 2013. Background and temperature effects on *Uca panacea* color change. Mar. Biol. 160, 1373–1381.
Levinton, J., Lord, S., Higeshide, Y., 2015. Are crabs stressed for water on a hot sand flat? Water loss and field water state of two species of intertidal fiddler crabs. J. Exp. Mar. Biol. Ecol. 469, 57–62.
Levinton, J., 2020. Thermal stress: the role of body size and the giant major claw in survival and heat transfer of a fiddler crab (*Leptuca pugilator*). J. Exp. Mar. Biol. Ecol. 530–531, 151428.
Mathewson, P.D., Moyer-Horner, L., Beever, E.A., Briscoe, N.J., Kearney, M., Yahn, J.M., Porter, W.P., 2017. Mechanistic variables can enhance predictive models of endotherm distributions: the American pika under current, past, and future climates. Global Change Biol. 23, 1048–1064.
Mouquet, N., Lagadeux, Y., Devictor, V., et al., 2015. Predictive ecology in a changing world. J. Appl. Ecol. 52, 1293–1310.
Munguia, P., Backwell, P.R.Y., Darnell, M.Z., 2017. Thermal constraints on microhabitat selection and mating opportunities. Anim. Behav. 123, 259–265.
Ockendon, N., Baker, D.J., Carr, J.A., et al., 2014. Mechanisms underpinning climatic impacts on natural populations: altered species interactions are more important than direct effects. Global Change Biol. 20, 2221–2229.
O'Connor, M.P., Spotila, J.R., 1992. Consider a spherical lizard: animals, models, and approximations. Am. Zool. 32, 179–193.
Pecl, G., Araujo, M.B., Bell, J.D., et al., 2017. Biodiversity redistribution under climate change: impacts on ecosystems and human well-being. Science 355, eaai9214.
Porter, W.P., Gates, D.M., 1969. Thermodynamic equilibria of animals with environment. Ecol. Monogr. 39, 227–244.
Porter, W.P., Mitchell, J.W., Beckman, W.A., DeWitt, C.B., 1973. Behavioral implications of mechanistic ecology. Oecologia 13, 1–54.
R Development Core Team, 2016. R: a Language and Environment for Statistical Computing. R Foundation for Statistical Computing, Vienna, Austria.
Riddell, E.A., Sears, M.W., 2015. Geographic variation of resistance to water loss within two species of lungless salamanders: implications for activity. Ecosphere 6, 86.
Riddell, E.A., Apanovitch, E.K., Odom, J.P., Sears, M.W., 2017. Physical calculations of resistance to water loss improve predictions of species range models. Ecol. Monogr. 87, 21–33.
Riddell, E.A., Roback, E.Y., Wells, C.E., Zamudio, K.R., Sears, M.W., 2019. Thermal cues drive plasticity of desiccation resistance in montane salamanders with implications for climate change. Nat. Commun. 10, 4091.
Smith, W.K., Miller, P.C., 1973. The thermal ecology of two south Florida fiddler crabs: Uca rapax Smith and Uca pugilator Bosc. Physiol. Zool. 46, 186–207.
Sonn, J.M., Porter, W.P., Mathewson, P.D., Richards-Zawacki, C.L., 2020. Predictions of disease risk in space and time based on the themal physiology of an amphibian host-pathogen interaction. Front. Ecol. Evol. 8, 576065.
Tatum, J., 2022. Celestial mechanics. LibreTexts e-book. Available at: https://phys.libretexts.org/Bookshelves/Astronomy_Cosmology/Celestial_Mechanics_(Tatum. (Accessed 26 January 2022). Last accessed.
Teal, J.M., 1959. Respiration of crabs in Georgia salt marshes and its relation of their ecology. Physiol. Zool. 32, 1–14.
Thomas, C.D., Cameron, A., Green, R.E., et al., 2004. Extinction risk from climate change. Nature 427, 145–148.
Thurman, C.L., 1998. Evaporative water loss, corporal temperature and the distribution of sympatric fiddler crabs (Uca) from South Texas. Comp. Biochem. Physiol. 119A, 279–286.
Urban, M.C., Bocedi, G., Henry, A.P., et al., 2016. Improving the forecast for biodiversity under climate change. Science 348, aad8466.
Vernberg, F.J., 1978. Metabolic response to thermal changes of the adult fiddler crab *Uca pugilator* and the effects of PCBs. Mar. Biol. 48, 135–141.
Wang, T., Hamann, A., Spittlehouse, D., Carroll, C., 2016. Locally downscaled and spatially customizable climate data for historical and future periods for North America. PLoS One 11, e0156720.
Wiens, J.J., 2016. Climate-related local extinctions are already widespread among plant and animal species. PLoS Biol. 14, e2001104.
Wilson, A.M., Jetz, W., 2016. Remotely sensed high-resolution global cloud dynamics for predicting ecosystem and biodiversity distributions. PLoS Biol. 14, e1002415.
Yoder, J.A., Tank, J.L., Rellinger, E.J., Moore, B.E., Gribbins, K.M., 2007. Differences in body size and water balance strategies between North Carolina and Florida populations of the sand fiddler crab, *Uca pugilator*. J. Crustac Biol. 27, 560–564.